Heliyon

Received:
6 September 2018
Revised:
14 November 2018
Accepted:
25 January 2019

Cite as: Takashi Maeshima, Keiichiro Oh-ishi. Solute clustering and supersaturated solid solution of AlSi10Mg alloy fabricated by selective laser melting.
Heliyon 5 (2019) e01186.
doi: 10.1016/j.heliyon.2019.e01186

Solute clustering and supersaturated solid solution of AlSi10Mg alloy fabricated by selective laser melting

Takashi Maeshima*, **Keiichiro Oh-ishi**

Toyota Central R&D Labs. Inc., Japan

* Corresponding author.
E-mail address: t-maeshima@mosk.tytlabs.co.jp (T. Maeshima).

Abstract

α-Al grains surrounded by Al-Si eutectic as the substructures in AlSi10Mg alloy fabricated by selective laser melting (SLM) were investigated in detail using three-dimensional atom-probe and transmission electron microscopy. Quantitative analysis of α-Al revealed (1) the formation of Mg clusters and Mg-Si co-clusters with a density in the order of 10^{23} /m^3 in α-Al of the as-built state caused by the complicated thermal history, and (2) a supersaturated Si content that significantly exceeded the maximum solubility due to rapid solidification, during the SLM process.

Keywords: Materials science, Inorganic chemistry, Metallurgical engineering

1. Introduction

Laser powder bed fusion (LPBF), commonly defined selective laser melting (SLM) is one of the additive manufacturing (AM) technologies that has attracted attention in recent years due to the achievement of high density by optimization of the process conditions and the high flexibility of design by layer by layer fabrication based on three-dimensional (3D) computer-aided design (CAD) models [1]. With the progress of this technology, manufacturing processes are shifting from conventional methods

https://doi.org/10.1016/j.heliyon.2019.e01186

to AM processes including SLM in some industries such as the aerospace and medical industries. Many investigations have been widely conducted on the topic of AlSi10Mg fabricated by SLM, such as (1) evaluation of the mechanical properties, microstructure, and fracture surfaces in different orientations to the building direction [2, 3, 4, 5], (2) characterization of textures depending on the scan strategy and detailed microstructural analysis [6, 7, 8], and (3) correlations between the mechanical properties of SLM samples subjected to heat-treatment conditions. Various heat treatments of SLM samples have been reported in the literature [9, 10, 11, 12]. These heat-treatment conditions were determined on the grounds of the phase diagram or conventional conditions for Al-Si-Mg ternary alloy fabricated by conventional processes. One of the characteristics of the as-built state of SLM samples is a fine microstructure of the supersaturated solid solution formed by a high cooling rate due to a small melt pool. The microstructure after solidification of molten material is repeatedly affected by subsequent laser paths. These heating by laser may cause precipitation and/or its precursor phenomenon during the SLM fabrication process of AlSi10Mg alloy. However, there are few reports on such microstructural changes at the nanometer scale [7]; therefore, guidelines for heat-treatment processes suitable for AlSi10Mg fabricated by SLM remain undisclosed. Accordingly, we investigate α-Al subgrains in detail as the smallest unit of the AlSi10Mg microstructure fabricated by SLM using transmission electron microscopy (TEM) and a 3D atom-probe (3DAP). We also investigate whether there is any clustering or precipitation and the quantitative supersaturation content of Si in the α-Al matrix in the as-built state.

2. Materials and methods

Cuboid SLM specimens with dimensions of 22 × 22 × 27 mm^3 were fabricated from AlSi10Mg powder supplied by LPW Technology whose chemical composition is reported as Al-9.9Si-0.34Mg-0.11Fe (wt%) and were processed used SLM 280 HL (SML solutions). The processing conditions for the fabrication of AlSi10Mg specimens in this study are given in Table 1. The laser moves in a zigzag pattern across the surface of a powder layer from one end to the other as shown in Fig. 1a. Another powder layer is then deposited on top of this layer, and the laser moves across the surface of the new layer with the scanned tracks rotated by 90° relative to the previous tracks. These steps are then repeated (Fig. 1a).

Table 1. Main processing parameters for the fabrication of AlSi10Mg specimens.

Laser power (W)	Scan speed (mm/s)	Hatch spacing (μm)	Spot diameter (μm)	Layer thickness (μm)
350	1150	170	80	50

https://doi.org/10.1016/j.heliyon.2019.e01186

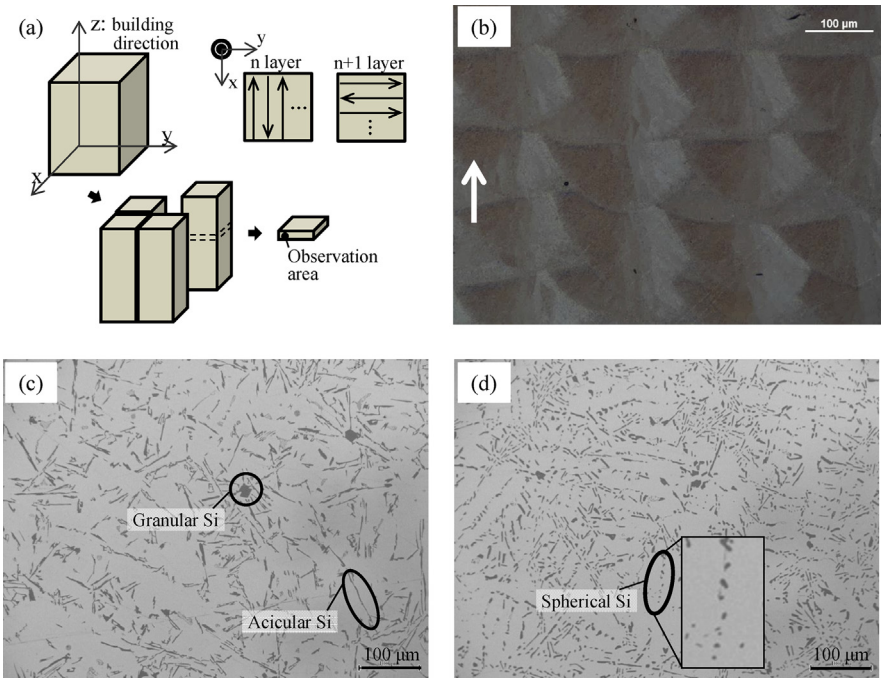

Fig. 1. OM micrographs of specimen cross sections. (a) Schematic illustration of a sample and the scan strategy. (b) OM image of as-built SLM alloy, (c) As-cast GDC alloy and (d) T6 heat-treated GDC alloy. The arrows in (b) indicate the building direction, z.

The microstructures were characterized using optical microscopy (OM), scanning electron microscopy (SEM), electron back scatter diffraction (EBSD), TEM, and 3DAP. In SLM process, when the powder layer is melted by the laser, the surface layer of the substrate just beneath it is also melted. The melting ratio of the powder layer and the substrate is not stable at the beginning of the process. On the other hand, remelting does not occur even immediately after completion of fabrication. For these reasons, the observation area for OM was located at a height of 15 mm from the bottom of the specimen. The specimen was divided into four, and the inside of the center was observed as shown in Fig. 1a. Samples used for SEM, TEM, and 3DAP were taken from the same location. The TEM samples were prepared by focused ion beam (FIB) machining (Hitachi NB-5000). Detailed microstructural observations were performed using a TEM (JEOL JEM-2100F) equipped with an energy dispersive X-ray spectroscopy (EDS) detector. Needle-like specimens for 3DAP (Cameca LEAP 4000X Si) analyses were prepared by FIB machining (FEI Helios 450). All 3DAP measurements were conducted in laser-pulsed mode with an evaporation rate of less than 0.1% ion/pulse at a base temperature of 70 K. The laser pulse energy used was 25 pJ. Mass spectra were confirmed due to concerns of Ga implantation in the specimens during FIB machining and the validity of the mass resolution. The Ga^+ peak was detected in the mass spectrum from the entire analyzed volume, while there was no Ga^+ peak in the mass spectrum from inside

https://doi.org/10.1016/j.heliyon.2019.e01186

of the analyzed volume. Therefore, Ga implantation from FIB machining was only at the surface, and cluster analyses were conducted using the analyzed volume without the surface region. A mass resolution of $M/\Delta M = 367$ of the Al^+ peak at the full-width at half-maximum (FWHM) was obtained using the analyzed volume without the surface region, which indicates sufficient resolution for the atom-probe analysis [13]. To investigate clustering, a detailed visual inspection of atom maps was performed using an established cluster search algorithm in the IVAS software [14].

Vickers hardness was measured with polished samples and determined using the average value of 5 independent measurements, except for the upper and lower limits. Hardness tests and OM observations were also performed for the as-cast and heat-treated (T6) AlSi10Mg samples, which were produced by gravity die casting (GDC) as a conventional process for comparison with the results of the SLM process.

3. Results and discussion

Fig. 1 shows OM images of microstructure viewed along the cross-section of AlSi10Mg fabricated by SLM (Fig. 1b) and GDC (Fig. 1c, 1d). The microstructure in Fig. 1b has typical laser tracks from SLM processing, as reported elsewhere [2, 3, 4, 5, 6, 8, 9]. Although the deposited powder for each layer correspond to 50 μm as shown in Table 1, the observed melting depth of track after melting looks close to ~100 μm since the surface layer of the substrate was also melted when the powder layer was melted by the laser. In contrast, granular particles and acicular Si with an Al matrix were observed in the as-cast alloy fabricated by GDC, as shown in Fig. 1c. The acicular Si was divided by T6 heat treatment and changed to spherical shape (Fig. 1d). The Vickers hardness of the samples is summarized in Table 2. The average Vickers hardness of the as-built SLM sample was 121 HV, which is twice that of the as-cast GDC alloy and almost as high as that of the heat-treated (T6) GDC alloy.

Thermodynamic calculation for Al-Si-Mg ternary system was conducted using the Thermo-Calc software package (2016a) with thermodynamic data from the SSOL4 thermodynamic database. Fig. 2 shows the phase diagram calculated for a vertical section of Al-xSi-0.35Mg and the calculated solidification path based on

Table 2. Vickers hardness of SLM and GDC AlSi10Mg samples.

Manufacturing method	SLM (as-built)	Gravity die casting	
		As-cast	T6
HV (200 gf)	121 ± 1	61 ± 2	114 ± 3

Error values are standard deviation σ

https://doi.org/10.1016/j.heliyon.2019.e01186

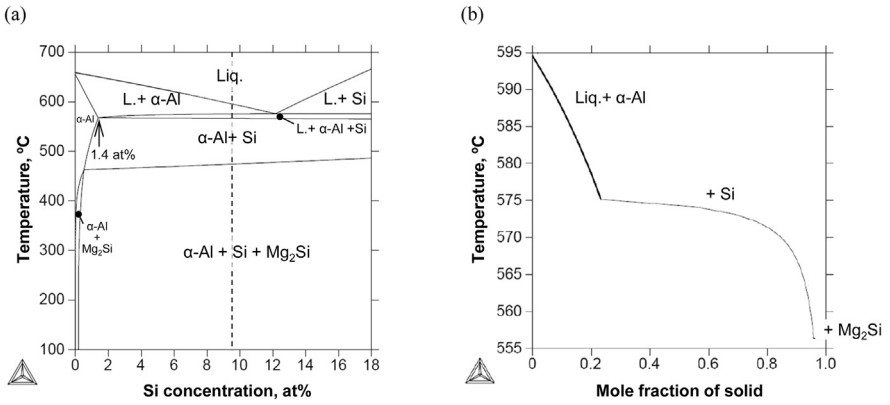

Fig. 2. (a) Calculated phase diagram for vertical section of Al-xSi-0.35Mg. The arrow in (a) indicates the maximum solubility value of Si (1.4 at%) in α-Al in the equilibrium state. (b) Calculated solidification path of Al-9.9Si-0.35Mg based on the Scheil-Gulliver model.

the Scheil-Gulliver model [15]. According to the calculated solidification path (Fig. 2b), primary α-Al grains are crystallized at the initial stage of solidification followed by Si. As the solidification progresses, solute atoms (Mg and Si) concentrate in the remaining liquid phase, then the liquid phase remains until low temperature as shown in Fig. 2b. Fine Mg_2Si is precipitated from α-Al during aging at 160 °C for 7 h, as indicated in the phase diagram since the phase diagram shows the most stable state (Fig. 2a). These precipitations contribute to the increase of hardness of GDC alloy after T6 heat treatment (Table 2). The relationship between the microstructure and hardness of the GDC samples can be easily understood from the thermodynamic equilibrium calculation, whereas it is difficult to explain the hardness of a sample fabricated by the SLM process. Crystallized Si was not evident from OM observations, as shown in Fig. 1b. Thus, it is conjectured that grain refinement and solid solution strengthening caused by rapid solidification lead to the superior hardness of the as-built SLM sample.

Analyses of the samples fabricated by SLM were conducted using SEM, EBSD, TEM, and 3DAP for detailed microstructural characterization. Fig. 3 shows SEM images of cross-sectional of the same sample as Fig. 1. The microstructure viewed along the cross-section perpendicular to the building direction shows in Fig. 3a. The inverse pole figure map in Fig. 3b using A1 direction (Normal Direction, ND) which is the perpendicular to the analysis surface shows that one laser scan track in the microstructure consists of elongated columnar and equiaxed grains, both of which contain a substructure of α-Al surrounded by Al-Si eutectic, as shown in Fig. 3c and 3d, respectively. The two substructures were observed to have a similar shape for their main structure of columnar and equiaxed grains. In the present study, the term "subgrains" will be used to distinguish from main grains such as elongated columnar and equiaxed grains. Elongated subgrains in columnar grains are 1−3 μm several micrometers long and 400−600 nm wide. The reason why the subgrains

https://doi.org/10.1016/j.heliyon.2019.e01186

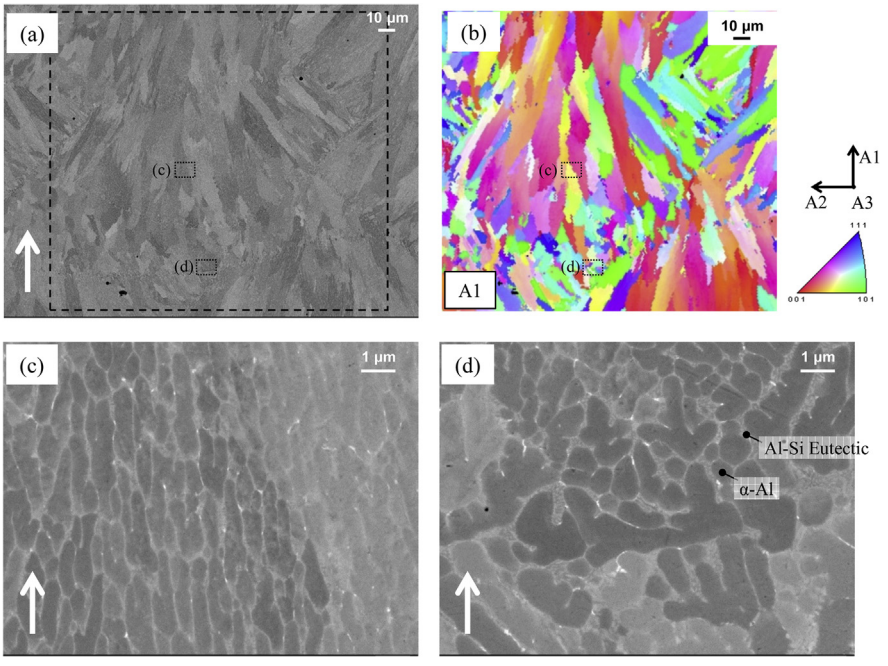

Fig. 3. SEM micrographs of sample cross sections. (a) Backscattered electron images of microstructure consisting of columnar and equiaxed grains showing the laser scan track. (b) Inverse pole figure orientation map from the dotted frame (a). (c,d) High-magnification images corresponding to regions (c) and (d) in (a). The arrows in (a, c, d) indicate the building direction, z.

are extended toward the building direction is that the subgrains grew along the heat flow direction. The OM image in Fig. 4a shows the region which samples were taken for TEM and 3DAP analyses. TEM and 3DAP samples were extracted from columnar grains, which occupied most of the microstructure in the SLM specimens. Fig. 4b shows a bright field TEM image of the subgrains. A plane perpendicular to the building direction was observed as indicated the mark to the left of Fig. 4b.

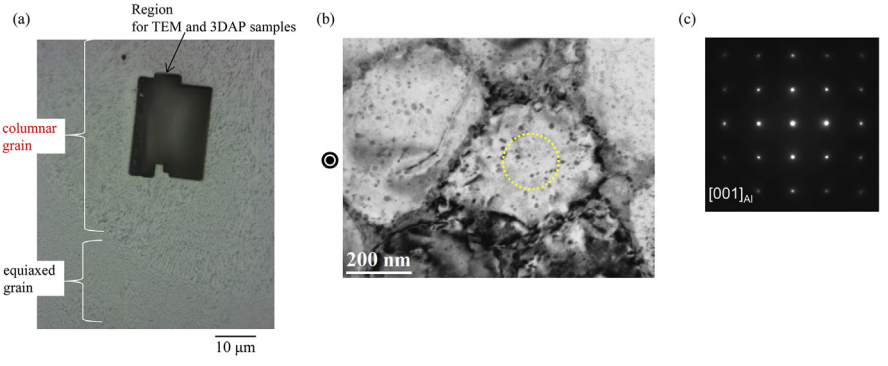

Fig. 4. (a) OM image of the region where TEM and 3DAP samples were extracted. (b) Bright-field TEM image of substructure. The mark to the left of the figure indicates the direction orthogonal to the building direction. (c) SAED pattern of α-Al matrix from the area indicated by the circle in (b). The beam direction is [001]Al.

https://doi.org/10.1016/j.heliyon.2019.e01186

The grain sizes of α-Al surrounded by Al-Si eutectic were 400−600 nm, which is consistent with the grain widths determined from SEM observation (Fig. 3c). Some dark dots were apparent within the α-Al grains (Fig. 4b). However, there were no extra reflection spots showing crystallization that corresponded to Si or Mg_2Si in the selected area electron diffraction (SAED) pattern in Fig. 4c taken along the <100> direction from the area indicated by the circle in Fig. 4b. From these results, it was found that some dark dots were neither due to precipitation nor crystallization of Si or Mg_2Si. which suggests that no precipitation or crystallization of Si or Mg_2Si occurred.

Fig. 5 shows a 3D atom map together with profiles across the α-Al/Al-Si eutectic interface of the specimen. For the concentration profiles, the atomic numbers were counted in cylindrical shape with gray color in Fig. 5a. The profiles show that the average Si content in α-Al was 2.2 at%, which is much larger than the maximum value in the equilibrium state of 1.4 at% calculated using Thermo-Calc, even at 577 °C (Fig. 2a), if all of these Si atoms are in a supersaturated solid solution. The concentration profiles also revealed that the average Mg content in α-Al was 0.1 at% and most of the Mg is segregated at eutectic region as shown in Fig. 5b. The results suggest that the Mg atom is segregated at the surface of Si particles between α-Al and Si since there is no solubility of Mg in Si.

Fig. 6a shows the 3DAP dataset of another sample with a large α-Al matrix region. The radial distribution functions (RDFs) of the bulk normalized concentration for each constituent around Si and Mg atoms in the α-Al matrix, taken from the cylindrical region indicated by the solid lines in Fig. 6a, are plotted in Fig. 6b and 6c, respectively. Bulk normalized concentration means that is scaled by average concentration of each element in the entire cylindrical region shown in Fig. 6a. Zhou et al. reported that RDF analysis is an effective tool to represent the interactions among

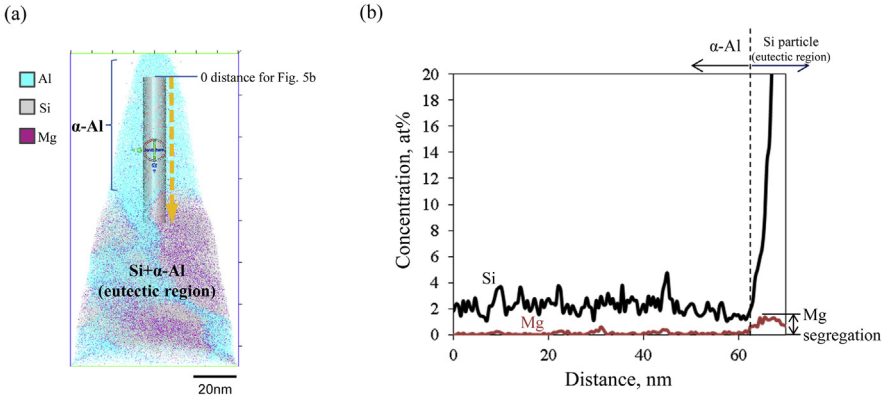

Fig. 5. (a) 3DAP atom map for all elements. (b) Composition profiles of Si and Mg across the α-Al/eutectic interface. The size of the sampling region for (b) in cylindrical shape with gray color in (a) is ∅ 11 nm × 70 nm.

https://doi.org/10.1016/j.heliyon.2019.e01186

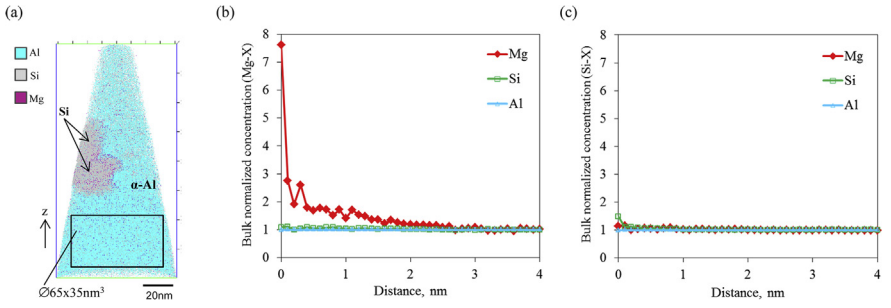

Fig. 6. (a) 3DAP elemental maps for all elements. (b,c) Radial distribution functions around Mg and Si atoms, respectively, taken from the cylindrical region in (a).

constituent atoms at the early stage of clustering [16]. Fig. 6b shows an excess of Mg atoms that tend to gather in the vicinity of the Mg atom. In contrast, the Si atom has little interaction with other Si atoms (Fig. 6c). These results suggest the formation of Mg clusters or Mg-Si co-clusters in α-Al during the SLM process. A solute nearest-neighbor (NN) analysis was conducted to reveal the distribution of solute atoms in α-Al. Fig. 7a shows the NN distribution of Mg atoms obtained from α-Al matrix taken from the cylindrical region in Fig. 6a and that expected from random distribution. "Random" means a natural distribution of the interatomic distances and "observed" means the analysis result of this work. The present result deviates from that for random distribution, and is shifted to a lower NN distance, which is evidence of clustering. Consequently, a cluster search algorithm was applied using the parameters $d_{max} = 1.25$ nm and $N_{min} = 4$. The clusters derived from the cylindrical region in Fig. 6a are presented in Fig. 7b. The clusters had an average diameter of 1.7 nm, assuming spherical clusters. The number of clusters in α-Al was 61 in the cylindrical region of $\varnothing 65 \times 35$ nm^3, which corresponds to a number density of 5.3×10^{23} /m^3. Fig. 7c shows the Mg/(Mg + Si) atomic ratio plotted as a function of the cluster volume. Approximately half are Mg clusters and the remaining are Mg-Si co-clusters. The alloy used in this study contained only 0.38 at% Mg. 3DAP analyses revealed that most of the small amount of Mg is accounted for by segregation at the surface of Si particles at the Si/α-Al interface, and by the formation of clusters. The small particles observed in the TEM image shown in Fig. 4b were confirmed as

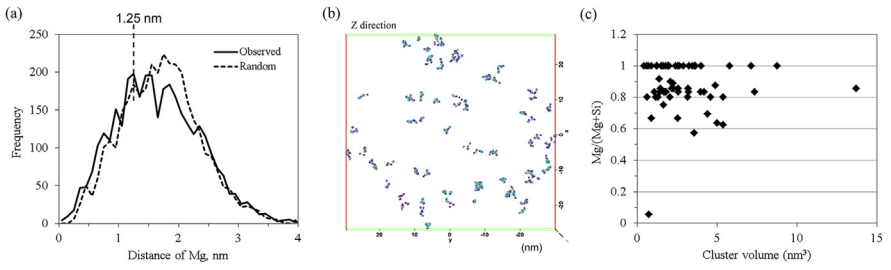

Fig. 7. (a) Solute NN analysis of Mg atoms. (b) Mg (light blue) and Si (purple) atom map showing solute clusters. (c) Mg/(Mg + Si) plotted as a function of the cluster volume.

https://doi.org/10.1016/j.heliyon.2019.e01186

Mg clusters and Mg-Si co-clusters because the SAED pattern (Fig. 4c) from the α-Al area only revealed face-centered cubic (FCC)-Al. Some small dots within the sub-grains in the as-built state were observed by TEM have been reported so far, however, it is not clear what these are [7]. In this paper, we have demonstrated these small dots are clusters.

The high strength or hardness of the SLM specimens in the as-built state has been reported to be due to grain refinement of the microstructure and the accompanying resistance to deformation of fine Si particles [7]. It was verified here that it is necessary to append the effect of the solid solution of Si, which has low solubility (less than 1.4 at% as shown in Fig. 2a) in α-Al due to the rapid cooling rate, to account for the high strength of as-built AlSi10Mg SLM specimens in addition to the previously reported mechanisms. Lattice deformation caused by the differences in atomic radii of Si (0.118 nm) and Al (0.143 nm) makes the movement of dislocations difficult [17]. The range of an introduced misfit in the hydrostatic stress field is directly proportional to the difference of atomic radius between FCC matrix and Si atoms. Therefore, sufficient solid solution strengthening could be obtained because the average amount of Si in α-Al was 2.2 at%, which significantly exceeds the solubility of Si in AlSi10Mg at room temperature. As reported earlier, α-Al cell contains about 2 at% Si using EDX, which was included silica caused by electro-polishing [7]. In contrast, it is estimated that α-Al contains 4 at% using XRD analysis [18]. Although there are some differences such as SLM machine for sample preparation, process condition and analysis method, at least what is common to these results is supersaturated Si content that significantly exceeded the maximum solubility due to rapid solidification during the SLM process. In the literature [18], specimens for analysis are also taken from the top surface of the fabricated sample. In this case, there is no remelting in surface so that the large supersaturated Si in α-Al is obtained than this study or Ref. [7]. Mg clusters and Mg-Si co-clusters in α-Al may provide additional strengthening in the as-built state; however, in the report on the cluster density in the heat treated Al alloy fabricated by the conventional method, the order of 10^{23} /m^3 does not contribute to the strength [19, 20, 21]. Hence, it is inferred that clusters in the SLM sample in this study do not directly contribute to strength in the as-built state. Having a different viewpoint, it is expected that these Mg clusters and Mg-Si co-clusters in SLM specimens with the as-built state accelerate the precipitation of Mg_2Si or Si as nuclei by subsequent low temperature and/or short-time heat treatments. The effect of clustering on the microstructural evolution in AlSi10Mg SLM specimens during aging should be studied as future research. It has been reported that Mg-Si co-clusters are formed in the 6000-family Al alloys (Al-Si-Mg) and 2000-family Al alloys (Al-Cu-Mg) by conventional wrought process [22, 23]. However, both single Mg clusters and Mg-Si co-clusters were observed in as-built state of SLM sample in this study. The reason why clustering occurred during the SLM process is not yet clear. The base temperature increases with the heated build

https://doi.org/10.1016/j.heliyon.2019.e01186

platform and the accumulation of laser paths during the SLM process. The temperature of the build platform is kept 373 K before fabrication of the AlSi10Mg SLM specimen in this study. In addition to the heat transfer from the build platform, the complicated thermal history owing to the cyclic laser scan and powder lamination layer was applied to the SLM specimens. It is assumed that one of the causes of clustering is such intrinsic thermal effect during the SLM process. Numerical calculations to simulate the complicated thermal history during the SLM process are required in order to find the cause of clustering [24, 25, 26].

4. Conclusions

α-Al subgrains as the smallest unit of the microstructure in AlSi10Mg fabricated by SLM were studied in detail. The main results are as follows.

(1) A typical laser track microstructure consists of elongated columnar and equiaxed grains in an SLM sample. The hardness of the as-built SLM sample is twice that of an as-cast GDC alloy and almost as high as that of a heat-treated (T6) GDC alloy.

(2) Both types of grains contain a substructure of α-Al surrounded by Al-Si eutectic. The formation of Mg and Mg-Si clusters with a density in the order of 10^{23} /m^3 in α-Al is considered to be caused by an intrinsic thermal effect during the SLM process.

(3) The average Si content in α-Al for an SLM sample was 2.2 at%, which significantly exceeds the solubility in the equilibrium state of AlSi10Mg. Solid solution strengthening contributes to the increased hardness of the SLM specimen.

Declarations

Author contribution statement

Takashi Maeshima: Conceived and designed the experiments; Performed the experiments; Analyzed and interpreted the data; Contributed reagents, materials, analysis tools or data; Wrote the paper.

Keiichiro Oh-ishi: Conceived and designed the experiments; Analyzed and interpreted the data; Contributed reagents, materials, analysis tools or data; Wrote the paper.

Funding statement

This research did not receive any specific grant from funding agencies in the public, commercial, or not-for-profit sectors.

https://doi.org/10.1016/j.heliyon.2019.e01186

Competing interest statement

The authors declare no conflict of interest.

Additional information

No additional information is available for this paper.

References

[1] D. Herzog, V. Seyda, E. Wycsick, C. Emmelmann, Additive manufacturing of metals, Acta Mater. 117 (2016) 371−392.

[2] D. Manfredi, F. Calignano, M. Krishnan, R. Canali, E.P. Ambrosio, E. Atzeni, From powders to dense metal parts: characterization of a commercial AlSiMg alloy processed through direct metal laser sintering, Materials 6 (2013) 856−869.

[3] I. Rosenthal, A. Stern, N. Frage, Microstructure and mechanical properties of AlSi10Mg parts produced by the laser beam additive manufacturing (AM) technology, Metallogr. Microstruct. Anal. 3 (2014) 448−453.

[4] E. Zaretsky, A. Stern, N. Frage, Dynamic response of AlSi10Mg alloy fabricated by selective laser melting, Mater. Sci. Eng. A 688 (2017) 364−370.

[5] F. Trevisan, F. Calignano, M. Lorusso, J. Pakkanen, A. Aversa, E.P. Ambrosio, M. Lombardi, P. Fino, On the selective laser melting (SLM) of the AlSi10Mg alloy: process, microstructure, and mechanical properties, Materials 10 (2017) 76−99.

[6] L. Thijs, K. Kempen, J.P. Kruth, J.V. Humbeeck, Fine-structured aluminium products with controllable texture by selective laser melting of pre-alloyed AlSi10Mg powder, Acta Mater. 61 (2013) 1809−1819.

[7] J. Wu, X.Q. Wang, W. Wang, M.M. Attallah, M.H. Loretto, Microstructure and strength of selectively laser melted AlSi10Mg, Acta Mater. 117 (2016) 311−320.

[8] N. Takata, H. Kodaira, K. Sekizawa, A. Suzuki, M. Kobashi, Change in microstructure of selectively laser melted AlSi10Mg alloy with heat treatments, Mater. Sci. Eng. A 704 (2017) 218−228.

[9] I. Rosenthal, R. Shneck, A. Stern, Heat treatment effect on the mechanical properties and fracture mechanism in AlSi10Mg fabricated by additive manufacturing selective laser melting process, Mater. Sci. Eng. A 729 (2018) 310−322.

https://doi.org/10.1016/j.heliyon.2019.e01186

[10] N.T. Aboulkhair, I. Maskery, C. Tuck, I. Ashcroft, N.M. Everitt, The microstructure and mechanical properties of selectively laser melted AlSi10Mg: the effect of a conventional T6-like heat treatment, Mater. Sci. Eng. A 667 (2016) 139–146.

[11] N.T. Aboulkhair, C. Tuck, I. Ashcroft, I. Maskery, N.M. Everitt, On the precipitation hardening of selective laser melted AlSi10Mg, Metall. Mater. Trans. A 46 (2015) 3337–3341.

[12] W. Li, S. Li, J. Liu, A. Zhang, Y. Zhou, Q. Wei, C. Yan, Y. Shi, Effect of heat treatment on AlSi10Mg alloy fabricated by selective laser melting: microstructure evolution, mechanical properties and fracture mechanism, Mater. Sci. Eng. A 663 (2016) 116–125.

[13] G. Sha, S.P. Ringer, Effect of laser pulsing on the composition measurement of an Al-Mg-Si-Cu alloy using three-dimensional atom probe, Ultramicroscopy 109 (2009) 580–584.

[14] A. Cerezo, L. Davin, Aspects of the observation of clusters in the 3-dimensional atom probe, Surf. Interface Anal. 39 (2007) 184–188.

[15] P. Schaffnit, C. Stallybrass, J. Konrad, F. Stein, M. Weinberg, A Scheil-gulliver model dedicated to the solidification of steel, CALPHAD 48 (2015) 184–188.

[16] J. Zhou, J. Odqvist, M. Thuvandar, S. Hertzman, P. Hedström, Concurrent phase separation and clustering in the ferrite phase during low temperature stress aging of duplex stainless steel weldments, Acta Mater. 60 (2012) 5818–5827.

[17] Aluminum-silicon casting alloys, Chapter 1, ASM International, 2004, pp. 7–9.

[18] S. Marola, D. Manfredi, G. Fiore, M.G. Poletti, M. Lombardi, P. Fino, L. Battezzati, A comparison of Selective Laser Melting with bulk rapid solidification of AlSi10Mg alloy, J. Alloy. Comp. 742 (2018) 271–279.

[19] Z.Q. Zheng, W.Q. Liu, Z.Q. Liao, S.P. Ringer, G. Sha, Solute clustering and solute nanostructures in an Al-3.5Cu-0.4Mg-0.2Ge alloy, Acta Mater. 61 (2013) 3724–3734.

[20] K. Buchanan, K. Colas, J. Ribis, A. Lopez, J. Garnier, Analysis of the metastable precipitates in peak-hardness aged Al-Mg-Si(-Cu) alloys with differing Si contents, Acta Mater. 132 (2017) 209–221.

[21] J.F. Nie, B.C. Muddle, On the form of the age-hardening response in high strength aluminium alloys, Mater. Sci. Eng. A 319–321 (2001) 448–451.

 https://doi.org/10.1016/j.heliyon.2019.e01186

[22] Y. Tang, W. Goro, S. Hirosawa, Z. Horita, S. Lee, K. Matsuda, D. Terada, Concurrent strengthening of ultrafine-grained age-hardenable Al-Mg alloy by means of high-pressure torsion and spinodal decomposition, Acta Mater. 131 (2017) 57−64.

[23] T. Sato, S. Hirosawa, K. Hirose, T. Maeguchi, Roles of microalloying elements on the cluster formation in the initial stage of phase diagram decomposition of Al-based alloys, Metall. Mater. Trans. A 34 (2003) 2745−2755.

[24] J. Yang, F. Wang, 3D finite element temperature field modeling for direct laser fabrication, Int. J. Adv. Manuf. Technol. 43 (2009) 1060−1068.

[25] C.H. Fu, Y.B. Guo, 3-dimensional finite element modeling of selective laser melting Ti-6Al-4V alloy, J. Manuf. Sci. Eng. 136 (2014) 1−7, 061004.

[26] W. Pei, W. Zhengying, C. Zhen, L. Junfeng, Z. Shuzhe, D. Jun, Numerical simulation and parametric analysis of selective laser melting process of Al-Si10Mg powder, Appl. Phys. A 123 (2017) 540−545.

https://doi.org/10.1016/j.heliyon.2019.e01186